Electronic materials

Determining internal porosity in Prussian blue analogue cathode materials using positron annihilation lifetime spectroscopy

Dominik Boras[1,*], Ida Nielsen[2,*] , Alexander Buckel[3], Tore Ericsson[2], Lennart Häggström[2], Reza Younesi[2], Torsten Stabb[1], and William R. Brant[2,*]

[1] *Chair of Chemical Technology of Materials Synthesis, University of Würzburg, Röntgenring 11, 97070 Würzburg, Germany*
[2] *Department of Chemistry - Ångström Laboratory, Uppsala University, Lägerhyddsvägen 1, 751 21 Uppsala, Sweden*
[3] *Altris AB, Kungsgatan 70b, 753 18 Uppsala, Sweden*

ABSTRACT

Prussian blue analogues (PBAs), $A_x M[M'(CN)_6]_{1-y} \cdot zH_2O$, are a highly functional class of materials with use in a broad range of applications, such as energy storage, due to their porous structure and tunable composition. The porosity is particularly important for the properties and is deeply coupled to the cation, water, and $[M'(CN)_6]^{n-}$ vacancy content. Determining internal porosity is especially challenging because the three compositional parameters are dependent on each other. In this work, we apply a new method, positron annihilation lifetime spectroscopy (PALS), which can be employed for the characterization of defects and structural changes in crystalline materials. Four samples were prepared to evaluate the method's ability to detect changes in internal porosity as a function of the cation, water, and $[M'(CN)_6]^{n-}$ vacancy content. Three of the samples have identical $[M'(CN)_6]^{n-}$ vacancy content and gradually decreasing sodium and water content, while one sample has no sodium and 25% $[M'(CN)_6]^{n-}$ vacancies. The samples were thoroughly characterized using inductively coupled plasma-optical emission spectroscopy (ICP-OES), thermogravimetric analysis (TGA), X-ray diffraction (XRD), and Mössbauer spectroscopy as well as applying the PALS method. Mössbauer spectroscopy, XRD, and TGA analysis revealed the sample compositions $Na_{1.8(2)}Fe^{2+}_{0.64(6)}Fe^{2.6+}_{0.36(10)}[Fe^{2+}(CN)_6] \cdot 2.09(2)H_2O$, $Na_{1.1(2)}Fe^{2+}_{0.24(6)}Fe^{2.8+}_{0.76(6)}[Fe^{2.3+}(CN)_6] \cdot 1.57(1)H_2O$, $Fe[Fe(CN)_6] \cdot 0.807(9)H_2O$, and $Fe[Fe(CN)_6]_{0.75} \cdot 1.5H_2O$, confirming the absence of vacancies in the three main samples. It was shown that the final composition of PBAs could only be unambiguously confirmed through the combination of ICP, XRD, TGA, and Mössbauer spectroscopy. Two positron lifetimes of 205 and 405 ps were observed with the 205 ps lifetime

Dominik Boras and Ida Nielsen have contributed equally to this work.

Address correspondence to E-mail: dominik.boras@uni-wuerzburg.de; ida.nielsen@kemi.uu.se; william.brant@kemi.uu.se

being independent of the sodium, water, and/or $[Fe(CN)_6]^{n-}$ vacancy content, while the lifetime around 405 ps changes with varying sodium and water content. However, the origin and nature of the 405 ps lifetime yet remains unclear. The method shows promise for characterizing changes in the internal porosity in PBAs as a function of the composition and further development work needs to be carried out to ensure the applicability to PBAs generally.

GRAPHICAL ABSTRACT
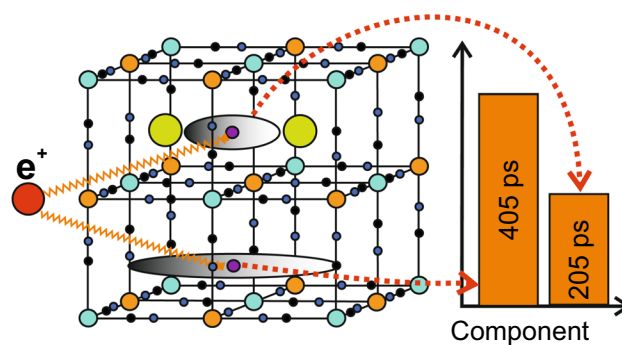
Introduction

Prussian Blue Analogues (PBAs), $A_xM[M'(CN)_6]_{1-y} \cdot zH_2O$ $A_xM[M'(CN)_6]_{1-y} \cdot zH_2O$, are an interesting class of materials for a broad range of applications due to their tunable composition and porous structure which in turn determine their properties. For example, in energy storage applications, such as sodium-ion batteries, PBAs are key candidates in terms of cost, environmental friendliness, and performance. Especially, the sodium-rich, low $[Fe(CN)_6]^{n-}$ vacancy iron-based PBA $Na_{2-4y-x}Fe[Fe(CN)_6]_{1-y} \cdot zH_2O$, also called Prussian white (PW), is a promising material. PW is inexpensive to prepare, consists of abundant elements, has a high theoretical sodium storage capacity (170.8 mAh/g for two sodium-ions extracted per formula unit), and a high voltage (3.2 V) [1, 2]. However, the sodium content, and thus the theoretical capacity, and the voltage output strongly depend on the $[Fe(CN)_6]^{n-}$ vacancy content. It should be mentioned that the use of the word "vacancy" in this study specifically refers to missing $[Fe(CN)_6]^{n-}$ complexes, while "mono-vacancy" refers to the absence of single atoms in the crystalline structure. To reach the maximum theoretical capacity in a full cell and reduce the poor electrochemical performance and structural degradation during cycling, a low $[Fe(CN)_6]^{n-}$ vacancy content ($y = 0$) is required which in turn gives a high sodium content ($x \to 0$ in the chemical formula, leading to a sodium content of 2) due to charge compensation [3, 4]. In addition to the sodium content, the presence of $[Fe(CN)_6]^{n-}$ vacancies also influences the water content. A high number of $[Fe(CN)_6]^{n-}$ vacancies results in additional porosity and the presence of bare metal sites to which water can coordinate. Since water can partake in unwanted side reactions with the electrolyte during cycling, leading to capacity fade, it is important that there are no water molecules ($z = 0$) within the structure [5]. Furthermore, the vacancy and water content are also found to influence the degree of ligand field splitting and therefore the electron orbital levels subsequently controlling the voltage profile of the material [6]. The $[Fe(CN)_6]^{n-}$ vacancy level can be controlled via the synthesis, especially the acid-facilitated self-decomposition synthesis has been reported to yield low-vacancy, sodium-rich PW [5, 7].

To determine the composition of PW and thus the vacancy content, methods such as inductively coupled plasma-optical emission spectroscopy (ICP-OES) and Mössbauer spectroscopy are commonly used. From ICP-OES, a C:Fe (or N:Fe) ratio of 3 indicates a vacancy-free material, a value lower than 3 implies the presence of vacancies, while a value higher than 3 implies the presence of impurities. Similarly, Mössbauer spectroscopy can be used to determine the vacancy level in PW by evaluating the spectral areas for low spin Fe_C and high spin Fe_N. If the spectral area

of high spin Fe_N is 50% (within errors) of the total Fe signal, it indicates that there are no $[Fe(CN)_6]^{n-}$ vacancies in the material as the $LS-Fe_C:HS-Fe_N$ ratio is 1:1. An additional versatile tool to study defects (mono-vacancies or metal-complex-vacancies) and structural changes in crystalline materials (metals, semiconductors, and ceramics) is Positron Annihilation Spectroscopy (PAS). Positrons are sensitive to both the electron density and electron momentum at their location within a crystalline or amorphous structure. In crystalline materials, they can probe structural defects like mono-vacancies, voids (larger clusters of vacancies), or metal-complex-vacancies [8, 9]. One specific PAS method is Positron Annihilation Lifetime Spectroscopy (PALS), where mainly the electron density is examined by measuring the lifetime of a positron inside a material. Since the positron lifetime is inversely proportional to the electron density at the localization site of a positron, defects like mono-vacancies, metal-complex-vacancies, or voids that have a lower electron density than the undisturbed perfect bulk material can be detected. PALS is capable of probing the defects present and enables the opportunity to quantify the density of those defects within a certain sensitivity range. In a few recent studies, it has been demonstrated that PALS can be used to distinguish defects in other material classes related to alternative battery systems to lithium-ion batteries (LIBs), thereby

providing added value for understanding these systems [10, 11]. Furthermore, Brunner et al. demonstrated that different charge states of an electrolyte can be measured [12]. However, for solid-state materials like cathodes, such investigations must be conducted postmortem since the penetration depth of positrons cannot be precisely confined to a point. PALS could be used to indirectly evaluate the State of Charge (SOC) of a battery comprised of PW since the sodium content is directly connected to the SOC. For example, if the initial sodium content is 2 per f.u. and after cycling the sodium content does not extend beyond 1.5 per f.u., this indicates that the battery is restricted to 75% SOC. In addition, the capacity is related to the composition, e.g., the capacity changes with the internal porosity going from 171 to 145 mAh/g when introducing $y = 0.1$ vacancies in $Na_{2-4y}Fe[Fe(CN)_6]_{1-y}$. Thus, the results from PALS can be related to the maximum theoretical capacity in terms of the internal porosity. For PW (Fig. 1), the structure changes as a function of the water and sodium content, while PBAs with $[Fe(CN)_6]^{n-}$ vacancies have cubic symmetry but contains larger internal porosity. The PALS method is not very sensitive to changes in the crystal structure, i.e., going from rhombohedral to cubic symmetry, however, if the average electron density in a perfect crystal does not change significantly, the PALS method should be very sensitive to the filling of
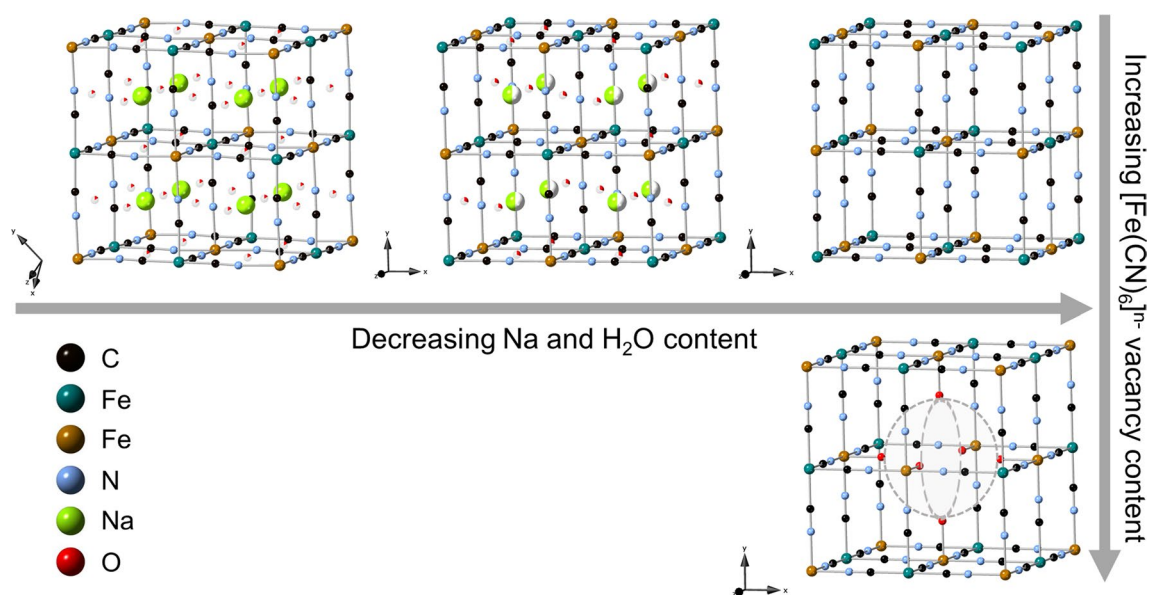

Figure 1 Structures of iron- and sodium-based PBAs as a function of the sodium, water, and $[Fe(CN)_6]^{n-}$ vacancy content. Positrons will mainly be located in the open channels within the

porous PBA framework to be furthest away from similar positively charged nuclei. The curved dotted lines highlight the void space formed when having $[Fe(CN)_6]^{n-}$ vacancies.

the open channels within the porous framework by sodium atoms or water molecules and/or the presence of $[Fe(CN)_6]^{n-}$ vacancies. This can then be related to the crystal structure obtained from X-ray diffraction (XRD).

Here, we present the first study where PALS is used to investigate PW samples with different sodium and water contents, and a Prussian blue (PB) sample with 25% $[Fe(CN)_6]^{n-}$ vacancies and no sodium present. The aim of this work is to benchmark the new PALS method applied to PBAs. Specifically, the sensitivity of PALS to samples of PBAs having different sodium, water, and/or $[Fe(CN)_6]^{n-}$ vacancy contents will be determined, while XRD will give the corresponding structure, TGA will give the water content, and Mössbauer spectroscopy and ICP-OES give the sodium content and the number of $[Fe(CN)_6]^{n-}$ vacancies present in the samples. The results revealed that the PALS method indeed can differentiate between PBA samples with varying sodium, water, and $[Fe(CN)_6]^{n-}$ vacancy contents with a rational trend in decomposition lifetimes, however, computational modeling is required to determine the nature of the different positron lifetimes. Furthermore, Mössbauer spectroscopy proves to be the best current practice to determine $[Fe(CN)_6]^{n-}$ vacancies and the sodium content in iron-based PBA cathode materials.

Methods

Synthesis

The pristine sample of fully sodiated Prussian white (FS-PW) was obtained from Altris AB. To make the samples with lower sodium content, two different synthesis methods were used. Firstly, to make half sodiated Prussian white (HS-PW), 1.0 g of FS-PW and 0.76 g of I_2 were dissolved in ~ 10 ml of acetone and stirred overnight under ambient conditions. The resulting powder was washed with acetone on filter paper and dried at 60 °C. Secondly, to make desodiated Prussian white (DS-PW), 1.0 g of FS-PW was mixed with 1.8 g NO_2BF_4 in 30 ml of acetonitrile in an Ar-containing glovebox for three days. The resulting powder (DS-PW) was washed three times with acetonitrile and centrifuged.

Prussian blue (PB-1) was made via a co-precipitation synthesis with $FeCl_3.6H_2O$ and $Na_4Fe(CN)_6$ as precursors both obtained from Sigma-Aldrich and used without further purification. The solutions were made with deionized water to get concentrations of 0.225 M for $FeCl_3 \cdot 6H_2O$ and 0.3 M for $Na_4Fe(CN)_6$ (4:3 ratio). The water used for $Na_4Fe(CN)_6$ was deoxygenated 1 h prior to mixing with powder. The solutions were slowly mixed (4 ml/h) with additional deionized water under constant stirring and airflow resulting in final concentrations of 28.1 mM for $FeCl_3 \cdot 6H_2O$ and 37.5 mM for $Na_4Fe(CN)_6$. The solution was stirred for 12.5 h with subsequent aging for 12.5 h. The aged powder was filtered and subsequently dried in a ventilated oven at 120 °C for 24 h.

Sample characterization

Sample compositions were determined using inductively coupled plasma-optical emission spectroscopy (ICP-OES) to determine relative Na and Fe content and elemental analysis to determine the C, H, and N content. The measurements were performed by Medac Ltd, United Kingdom. The water content was determined using thermogravimetric analysis (TGA) on a TA Instruments TGA5500. ~ 5 mg of powder was loaded onto a Pt pan in air before placing the sample onto the TGA furnace under flowing N_2 (25 ml/min). The sample was then heated to 350 °C with a heating rate of 1 °C/min. Particle size and morphology were determined using scanning electron microscopy (SEM) on a SEM/EDS-Zeiss 1550 instrument working with an acceleration voltage of 3 kV with a working distance of 4.3 mm using an in-lens detector. The samples were loaded onto carbon tape and transferred into the vacuum chamber of the microscope.

The structure of the samples was investigated using powder X-ray diffraction (XRD). The samples were prepared for laboratory XRD by placing the powder on a powder holder surrounded by a Si disk. The XRD measurements were performed on a Bruker D8 Twin Twin diffractometer (double Cu Kα radiation $\lambda_1 = 1.540600$ Å, $\lambda_2 = 1.544390$ Å) with a Lynx-eye XE-T position sensitive detector. The experiments were conducted between 10° and 80° in steps of 0.02°. The obtained diffraction patterns were fitted using the Pawley method in the TOPAS academic software

[13] to determine the space group symmetry and cell parameters.

Mössbauer measurements were carried out at room temperature on a spectrometer with a constant acceleration type of vibrator and a ^{57}CoRh source. The samples were enclosed in a sealed Kapton cover. The so-formed absorbers had a sample concentration of ~ 7–10 mg/cm^2. Calibration spectra were recorded at 295 K using natural Fe metal foil as a reference absorber. The spectra were folded and fitted using the least square Mössbauer fitting program Recoil to obtain the values of the center shift CS, the magnitude of the electric quadrupole splitting IQSI, the full-width at half maxima W of the Lorentzian absorption lines, and the spectral areas A.

Sample preparation for PALS

The positron source used was the isotope ^{22}Na encapsulated with thin (7.5 μm thick) Kapton foil on both sides [14]. To determine the fraction of annihilation events stemming from the source (^{22}Na and covering foil), a pure aluminum sample was measured. The reason for this choice is the average nuclear charge of 13 in Al, which is close to that of 9.5 in PW. The fraction of events stemming from the source was determined to consist of the following lifetime components: 372.42 ps (foil) and 2896.39 ps (positronium from enclosed air and/or stemming from the glue ring of the foil). These components have the following relative intensities: 0.1242 and 0.0031, respectively. The difference to 1 is related to annihilation events in the Al sample. For all measurements of the PBA samples, the source was positioned in a specially made aluminum box covered from both sides by an equally thick layer of the sample material ensuring that the source is approximately placed in the middle of the box (Figure S1). Thus, it was ensured that no positrons could escape from the box, which would result in contaminations of the spectra from unwanted events. Powders with an average powder particle diameter above 10 μm were chosen for PALS experiments as it ensures that only a negligible part (less than 0.1%) of the implanted positrons can reach the surfaces of the powder particles [9]. Thus, the formation of positronium at the surface is negligible. The sample box was then placed between two Hamamatsu H1949-50 photomultiplier tubes with scintillators mounted on the optical window. The scintillator material used was plastic BC

422Q-0.5wt., which gives an easy-to-handle instrumental resolution function [15]. To have good statistics for the evaluation of the spectra, at least 5 million counts in a single spectrum were recorded. This ensures, together with the applied pulse filtering, spectra that are nearly free of artifacts, e.g., pile-up events. Thus, the spectra show a very reliable decomposition into several lifetime components [15].

Data acquisition in PALS

Positron annihilation lifetime spectroscopy was performed employing a semi-digital setup as described in Petschke et al. [15]. The system consisted of an analog photodetection system combined with digital hardware. Non-coincident events are filtered in the first stage by analog electronics employing constant fraction discriminators. All coincident pulses were then digitized by the DRS4-Eavluation Board [16]. The analog photodetection system consisted of two colinearly arranged (180°) Hamamatsu (H1949-50/WA-5309) photomultiplier tubes (PMTs). Conically shaped plastic BC422Q crystals were used as scintillators, which had been glued to the PMTs with Wacker silicone oil (AK10000) to ensure optimal optical contact. When the DRS4 evaluation board receives the external trigger from the two Constant Fraction Discriminators (CFDs), the capacitor arrays are successively charged by the pulses employing a sampling rate of 5.12 GHz with a sweep of 200 ns. The stored pulses are then digitized by an 80 MHz ADC (14 bit) and read out by a PC via a USB 2.0 interface. Moreover, to adjust the analog input range to ± 500 mV, the pulses are attenuated by − 20 dB. To reduce noise, the DRS4 Board was calibrated as described in earlier work [17].

Analysis of PALS spectra

The experimentally obtained lifetime spectra were analyzed by employing the software tool DQuickLTFit v4.2 as described in earlier work [18]. The employed model commonly used for fitting lifetime spectra consists of an analytical solution of a sum of N exponentially decaying functions, which is convoluted with a sum of Gaussians mimicking the instrumental response function. This approach was first published by Kirkegaard et al. in its mathematical formulation [19]. Moreover, the MPFIT library is implemented in DQuickLTFit [20] for solving the nonlinear least-square problem employing the Levenberg—Marquardt algorithm [21, 22].

Results

Composition, crystal structure, particle size, and morphology

ICP analysis of FS-PW revealed the composition $Na_{2.34(6)}Fe[Fe(CN)_6] \cdot zH_2O$ implying an excess of sodium (Table S1). The TGA measurement of FS-PW (Figure S2) shows a weight loss of ~ 10.8% in the temperature range 30–250 °C, which corresponds to surface absorbed water and interstitial water [2.09(2) per formula unit (f.u.)]. Similarly, the composition of HS-PW and DS-PW were determined from ICP and TGA analysis to be $Na_{1.52(5)}Fe[Fe(CN)_6] \cdot 1.57(1) H_2O$ and $Na_{0.19(3)}Fe[Fe(CN)_6] \cdot 0.807(9)H_2O$, respectively. All PW samples have similar cubic morphology with micron-sized particles (Figure S4A-F). The TGA curve of PB-1 (Figure S3) is very similar to previous literature on PB [23] giving an indirect indication of the presence of $[Fe(CN)_6]^{n-}$ vacancies. A 25% $[Fe(CN)_6]^{n-}$ vacancy content gives the formula $Fe[Fe(CN)_6]_{0.75}$, however, in the following discussion of the TGA results for PB-1, in order to remain comparable to previous literature, the $Fe_4[Fe(CN)_6]_3$ formula is used. This also corresponds to the atomic content of a single unit cell. Similar to previous reports, three distinct mass losses in the temperature range from 30–288 °C are observed. To interpret the TGA results, we assume a 25% $[Fe(CN)_6]^{n-}$ vacancy content. The first mass loss of 4.8% (30–128 °C) corresponds to two water molecules per $Fe_4[Fe(CN)_6]_3$ that are connected via hydrogen bonds to the metal-bound water molecules. The second mass loss of 8.7% (128–237 °C) corresponds to four water molecules per $Fe_4[Fe(CN)_6]_3$ that are bound to the bare metal sites available within the structure due to the presence of $[Fe(CN)_6]^{n-}$ vacancies. The third mass loss of 6.8% (237–288 °C) corresponds to the last of the metal-bound water molecules and the decomposition of the material, i.e., cyanide loss. It is assumed that there should be at least six water molecules per $Fe_4[Fe(CN)_6]_3$ as there are six bare metal sites per unit cell. However, to unravel exactly how much water and other decomposition products that are lost during this temperature range, TGA combined with mass spectrometry is necessary. The initial mass losses observed in this study are, however, in line with previous results [23]. ICP analysis of PB-1 revealed some sodium present in the sample [2.3(3) wt%] corresponding to 0.30(2) sodium-ions per $Fe[Fe(CN)_6]_{0.75}$. This is not expected in PB, thus, the additional sodium must arise from an impurity, e.g., from the synthesis precursor. The PB-1 sample consists of agglomerates of smaller nano-sized particles (Figure S4G-H).

Laboratory XRD was performed to determine the structures of the samples (Figure S5). FS-PW adopts a rhombohedral $R\bar{3}$ structure in line with previously reported room temperature measurements on PW [24]. DS-PW adopts a cubic $Fm\bar{3}m$ structure also in line with previously reported structures for low sodium content PW [25]. Interestingly, the sodium content of 1.52(5) determined from ICP for HS-PW should correspond to a mixture of cubic $Fm\bar{3}m$ and rhombohedral $R\bar{3}$ phases since a sodium content of 1.52(5) lies in the two-phase region for PW (~ 1.2 to ~ 1.8 sodium-ions per f.u.) [26]. However, the material adopts a cubic $Fm\bar{3}m$ structure. Thus, this result adds further evidence to the conclusion from ICP on FS-PW that there is an excess of sodium. However, as no additional phases were observed in the XRD patterns, the additional sodium must arise from an amorphous compound. PB-1 adopts a cubic $Fm\bar{3}m$ structure in line with previous studies of PB [27].

Mössbauer spectroscopy

Due to the ambiguity about the sample compositions arising from comparing the ICP and XRD results, Mössbauer spectroscopy was applied to bring further clarity. Namely, the sodium content in iron-based PBAs can be determined through the determination of the valence sum of the two iron centers. The spectra of FS-PW, HS-PW, and DS-PW measured at 295 K are shown in Fig. 2. The Mössbauer spectra of FS-PW and HS-PW are fitted with three doublets, while the spectrum of DS-PW is fitted with two doublets. The fitting parameters are presented in Table S2. The assignments of Mössbauer patterns to different Fe sites are done according to previously reported spectra of PW [7, 25, 28]. The patterns with negative CS values are originating from low spin Fe coordinated by six C atoms (denoted Fe_C), and the patterns a and b originate from high spin Fe coordinated with six N atoms (denoted Fe_N). For DS-PW, which has very low water and sodium contents, both Fe_C and Fe_N are three valenced indicating no sodium present in the sample as opposed to the ICP result. The hyperfine parameters agree well with previously reported Mössbauer spectra [25].

Typically for hydrated PW, two Mössbauer patterns are observed: One originating from low spin Fe_C^{2+} and
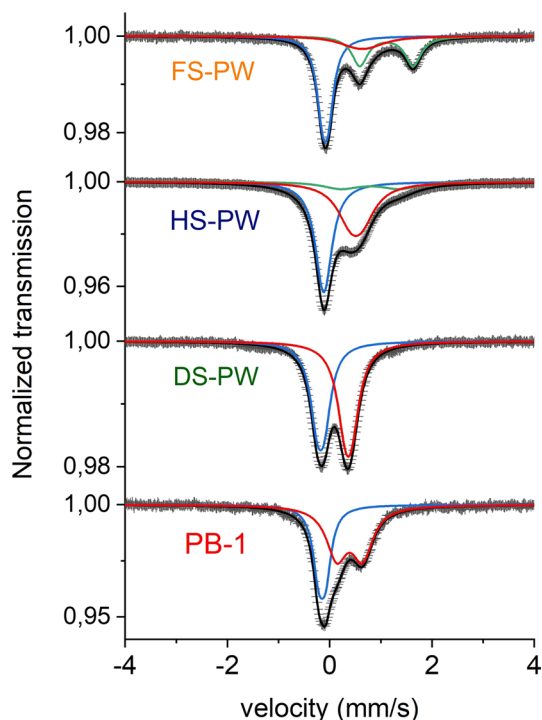
Figure 2 Mössbauer spectra measured at 295 K of FS-PW, HS-PW, DS-PW, and PB-1. The blue subpattern originates from low spin Fe_C, while the green (corresponding to pattern a for FS-PW and HS-PW) and red (corresponding to pattern b for FS-PW and HS-PW) subpatterns originate from high spin Fe_N.

one originating from high spin Fe_N^{2+} [7]. For FS-PW in the present study, which has a rhombohedral $R\bar{3}$ structure, one pattern originating from low spin Fe_C^{2+} is observed. Two patterns originating from high spin Fe_N^{2+} are observed: One main pattern a which can be interpreted as 2+ valenced and one minor pattern b. The main pattern a has hyperfine parameters similar to the parameters previously reported for hydrated PW (Table S2) [7]. The pattern b with CS = 0.64(5) mm/s and a quadruple splitting of 0.27(22) mm/s, however, does not match with previous reported results. This pattern cannot originate either from high spin Fe_N^{2+} or Fe_N^{3+} but is more likely from high spin Fe_N with a valence state between 2+ and 3+. Patterns with CS values in this order have earlier been interpreted as originating from Fe with an electronic relaxation time shorter than the Mössbauer observation time. In fact, it has been shown that reducing the temperature at which the spectra are recorded has resulted in longer relaxation times and given resolved Fe^{2+} and Fe^{3+} patterns [29]. By interpolating the CS value between the Fe_N^{2+} value for FS-PW [1.111(6) mm/s] and the Fe_N^{3+}

value for DS-PW [0.365(2) mm/s], results in an average Fe_N valence value of 2.6+ for pattern b for FS-PW. Therefore, it is reasonable to assume that the sodium content is less than two per f.u. in FS-PW. An alternative interpretation of the result is that the presently reported structure $R\bar{3}$ for FS-PW is different to earlier work on monoclinic $P2_1/n$ PW [7]. According to the crystallographic data published by Nielsen et al. [24], the average Fe nearest neighbor distances are Fe_N = 2.158(3) Å and Fe_C = 1.905(4) Å for the monoclinic $P2_1/n$ structure and Fe_N = 2.147(1) Å and Fe_C = 1.912(1) Å for the rhombohedral $R\bar{3}$ structure. The local Fe environments in the $R\bar{3}$ structure are closer to a regular symmetric octahedral environment, otherwise, the differences between the two room temperature structures are small. From these considerations, minor variations are expected in the hyperfine parameters CS and IQSI extracted from the Mössbauer spectra for the two room temperature structures of PW. Using the spectral areas as an indication of the number of different valences for Fe in the sample, the following formula using the charge neutrality criteria can be deduced for FS-PW (excluding water): $Na_{1.8(2)}Fe_{0.64(6)}^{2+}Fe_{0.36(10)}^{2.6+}[Fe^{2+}(CN)_6]$.

The spectrum for HS-PW is similar to the spectrum of cubic PW with a sodium content of 1.0 and a water content of 1.79 previously reported [25]. The pattern a has an Fe_N^{2+} valence while the pattern b originates from high spin Fe_N having a valence between 2+ and 3+. Using the same argument as above for pattern b, the Fe_N valence would be 2.8+ for HS-PW. Turning to the Mössbauer pattern of Fe_C with a CS value of −0.112(2) mm/s, which is in between −0.084(2) mm/s for Fe_C^{2+} in FS-PW and −0.177(2) mm/s for Fe_C^{3+} in DS-PW, gives an average valence for Fe_C of 2.3+ for HS-PW (using linear interpolation between the two CS values for FS-PW and DS-PW). Using the charge balance criteria, the following formula for HS-PW is deduced (excluding water): $Na_{1.1(2)}Fe_{0.24(6)}^{2+}Fe_{0.76(6)}^{2.8+}[Fe^{2.3+}(CN)_6]$.

The spectrum for PB-1 is shown in Fig. 2 with fitting parameters presented in Table S2. The assignment of the Mössbauer patterns to the different Fe sites are done in accordance with earlier work on PB samples done by Reguera et al. [30]. Firstly, the amount of Fe on the different sites is evaluated. The spectral areas are 60(3)% and 40(3)% for Fe_N and Fe_C, respectively. This is in good agreement with occupation areas of $Fe[Fe(CN)_6]_{0.75}$ in earlier work [30]. However, when calculating the Fe occupancies from the spectral areas,

two effects have to be taken into account: absorber thickness effects and the possibility of any difference in the recoil-free factors f for Fe_N and Fe_C. To evaluate if the spectral areas depend on the absorber thickness, a thinner absorber with 5 mg/cm^2 of sample was made. The spectral areas did not change, thus, the absorber thickness effects do not appear. The possibility of differences in f-factors were not tested in this study, but is believed to have an insignificant effect since the spectral areas in this study are very similar to the spectral areas (57%/43%) from Reguera et al. [30]. Secondly, the hyperfine parameters CS and IQSI are evaluated. The values can be assigned to high spin Fe_N^{3+} and low spin Fe_C^{2+} in good agreement with earlier work [30]. We do not observe any pattern related to high spin Fe_N^{2+}, which would have a much larger CS value (ca. 1.1 mm/s) [23]. The pattern for Fe_N^{3+} is in principle a superposition of a pattern from Fe_N^{3+} surrounded by six N atoms in octahedral coordination and a pattern from Fe_N^{3+} surrounded by four N atoms and two water molecules (bound to Fe via the oxygen atom) in octahedral coordination. If the water content is larger than 1.5 per $Fe[Fe(CN)_6]_{0.75}$, these two patterns would have an intensity ratio of 3:1 according to the structure of PB (Fig. 1). In this case, however, the resolution of the Mössbauer spectra is limited, and thus, the two high spin Fe_N^{3+} patterns cannot be resolved. Nonetheless, the larger line width of the Fe_N pattern relative to the Fe_C pattern (Table S2) reflects the different surroundings for Fe_N. This result can also be interpreted in relation to previously reported Berlin Green (BG, $Fe^{3+}[Fe^{3+}(CN)_6]$) which has no vacant Fe_C atoms in the structure [25]. In PB-1, the low spin Fe_C^{2+} has a center shift value of − 0.147(5) mm/s while in BG, the low spin Fe_C^{3+} has a center shift value of −0.18(1) mm/s. For high spin Fe_N, the CS values for PB-1 and BG are similar (Table S2) being three valenced. The much larger IQSI value for high spin Fe_N for PB-1 as compared to BG [0.51(2) mm/s and 0.05(1) mm/s, respectively] reflects the two different surroundings for high spin Fe_N in PB-1 as discussed above. Finally, the charge balance in PB-1 is evaluated. The valence for all Fe_N is 3+, while the valence for Fe_C is 2+. Thus, the total Fe charge is 18+ and balances exactly with the total negative charge of the cyanide. Therefore, there is no need for any extra sodium-ions to obtain charge neutrality in this sample. This cast doubts about the sodium content detected by ICP, which must come from an impurity.

In summary, the found sodium contents from Mössbauer spectroscopy are lower by 0.54(6) for FS-PW and 0.42(5) for HS-PW relative to the values obtained from ICP. Therefore, a consistent result is that amorphous sodium impurities are responsible for ~ 0.48(4) of the measured sodium content, while for DS-PW and PB-1 it is responsible for ~ 0.19(3) and ~ 0.30(2), respectively, of the measured sodium content. Finally, the Mössbauer results showed that no $[Fe(CN)_6]^{n-}$ vacancies are present in the three PW samples, while there are 25% $[Fe(CN)_6]^{n-}$ vacancies in the PB-1 sample confirming the correct assumption made when interpreting the TGA results.

Positron annihilation lifetime spectroscopy

A common problem for PBAs is to quantify the number of $[Fe(CN)_6]^{n-}$ vacancies, which strongly influence the material properties. To gain additional information on the internal porosity, the PALS method is for the first time applied to four PBA samples with varying sodium, water, and $[Fe(CN)_6]^{n-}$ vacancy contents.

Firstly, the average lifetime was determined, which gives a general statement of the change in the electron density at the localization sites of the positrons. It can be seen from Fig. 3 that the average lifetime decreases significantly with increasing sodium and water content. For DS-PW, a value of $\tau_{av} = (396.7 \pm 3.4)$ ps was obtained, while for HS-PW it was determined to be $\tau_{av} = (348.6 \pm 3.5)$ ps and, finally, for FS-PW, the value
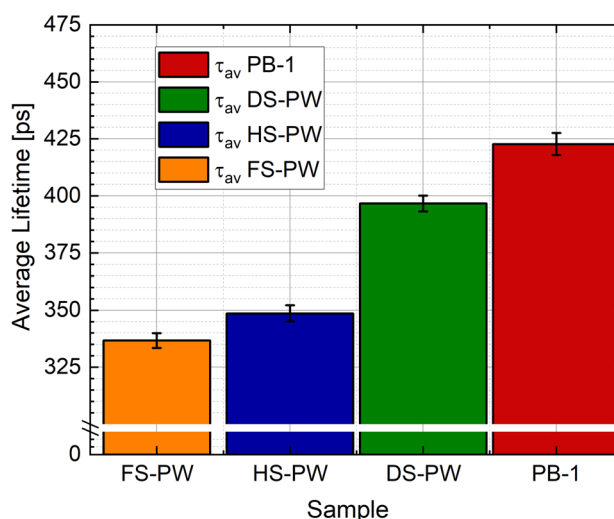
Figure 3 Average positron lifetime for PB-1 (422.7 ± 4.8) ps, DS-PW (396.7 ± 3.4) ps, HS-PW (348.6 ± 3.5) ps and FS-PW (336.7 ± 3.3) ps.

is $\tau_{av} = (336.7 \pm 3.3)$ ps. The average lifetime for the PB-1 sample, which contains $[Fe(CN)_6]^{n-}$ vacancies, was found to be $\tau_{av} = (422.7 \pm 4.8)$ ps. In the positron community, a change in the average positron lifetime of more than 2 ps is considered reliably related to changes in the microstructure of the investigated samples. Here, changes between 12 and 48 ps from one sample to the other are observed, which is considered a significant change in the average lifetime. Figure 1 shows the structures of PW as a function of the sodium and water contents and the structure of PB-1, a sample with a high defect density due to the presence of $[Fe(CN)_6]^{n-}$ vacancies. When the composition and/or structure of PW changes, the radius of the open channels in the porous PBA framework changes, and, accordingly, also the electron densities should change. When having $[Fe(CN)_6]^{n-}$ vacancies present, the internal porosity increases additionally to the open channels. If one evaluates the respective PALS data with a free fit, τ_1 is ∼ 205 ps for the PW samples, while τ_2 increases from (369.3 ± 1.3) ps for FS-PW to (458.4 ± 2.0) ps for DS-PW (Table S3). Since all three PW samples have a lifetime component of 205 ps within error, one positron lifetime equal to 205 ps was chosen for the fixed lifetime evaluation. In the PB-1 sample, containing a very high percentage of defects, two lifetimes of τ_1 (217.9 ± 3.7) ps and τ_2 (471.4 ± 1.2) ps were observed. The first lifetime differs by about 10 ps relative to the PW samples, nevertheless, the determined χ^2 is within a reasonable range around 1, when the first component is fixed at 205 ps (Table S4). It should be mentioned that even though PB-1 has a high defect density resulting in a higher porosity relative to the PW samples, the high porosity is lost again as the defects are filled with water molecules. Additionally, in the case of DS-PW and PB-1, a very long third component in the range of 2500 ps was also observed when fixing the first component. However, it has a very low intensity and consequently only contributes to a very small fraction of the average positron lifetime. This

component could indeed stem from a surface effect or an additional source component because of the difference in particle size. Since the second characteristic positron lifetime component, τ_2, changes slightly over all three samples (Table S4), an average value of 405 ps was chosen to be fixed, thus ensuring that the relative intensities become meaningful. Figure S6 shows as an example of a fit evaluation employing two free positron lifetime components for the sample HS-PW. Here, it is clear that the residuals behave in a proper range and the spectrum is of high quality.

Having a closer look at the two-component fit, it was found that each decomposition of the spectra gives a χ^2 value close to 1 (Table 1) indicating that fitting only two lifetime components is a valid assumption. However, a free fit (all parameters, i.e., lifetime and intensities, are left for varying) often results in different positron lifetime values in the range of 10 ps for the second component and, thus, it is difficult to compare the corresponding intensities of these components. Hence, the two lifetimes were fixed to 205 and 405 ps to better compare the four samples with each other. It can be seen in Fig. 4 that the intensity corresponding to the component with the longer lifetime (405 ps) decreases going from no or low sodium content to high sodium content. This indicates that the fraction of positrons annihilating with a shorter characteristic lifetime is increasing with increasing sodium and water content. The intensity corresponding to the shorter positron lifetime component (205 ps) increases with increasing sodium and water contents. This can be explained by the fact that inside the open channels, the distance between the sodium atoms becomes smaller as more sodium occupies the channels. Consequently, this leads to a higher electron density in the open channels and, thus, a shorter lifetime for positrons located there when more sodium and water are present in the structure. In the PB-1 sample with a high concentration of metal-complex-vacancies, a third component (∼ 514.2 ps) with a high intensity

Table 1 Decomposition of positron lifetime spectra with two lifetime components (205 ps and 405 ps) fixed

Sample	τ_1 (ps)	I_1	τ_2 (ps)	I_2	τ_3 (ps)	I_3	χ^2
FS-PW	205	0.364	405	0.636	0	0	1.086
HS-PW	205	0.280	405	0.720	0	0	0.977
DS-PW	205	0.155	405	0.770	863.1± 9.9	0.075	1.108
PB-1	205	0.141	405	0.431	514.2± 5.1	0.428	0.908

All fits show a χ^2 close to 1. For DS-PW, a third long-lived component with a small intensity was measured. For the PB-1 sample, a component at (514.2 ± 5.1) ps was measured
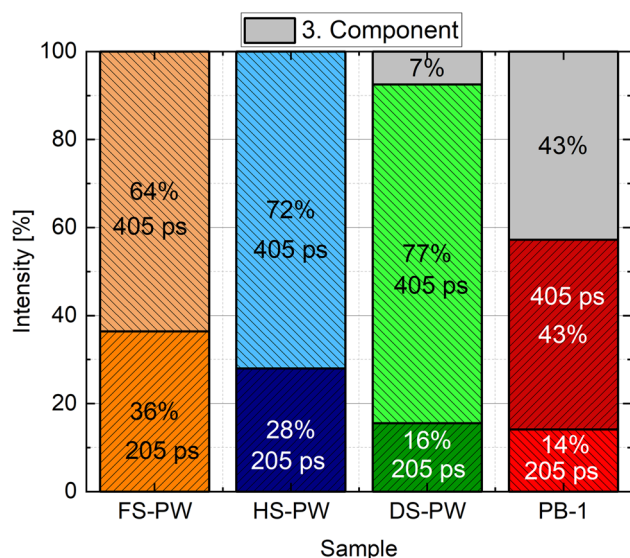
Figure 4 Lifetime components found for the four samples. For all four samples, a decomposition of the lifetime spectra is recorded, where χ^2 reaches a value close to 1 indicating a correct number of components involved in the fitting. For convenience, the third long-lived component observed for DS-PW and PB-1 is shown as a gray bar.

was observed. Therefore, the intensities are difficult to compare with this sample but indicate another dominant positron trap.

Discussion

Based on the analysis performed to verify the compositions of the samples, an evaluation of the different methods, especially the applicability of the PALS method to determine the internal porosity of PBAs with changing sodium, water, and $[Fe(CN)_6]^{n-}$ vacancy content, is given.

From the ICP result of the pristine sample FS-PW, an excess of sodium was found. However, it is very unlikely to have more than two sodium-ions per f.u. in iron-based PBAs as it would imply Fe being in oxidation state +1. Furthermore, when comparing the structure of HS-PW determined from XRD with the ICP results, the cubic $Fm\bar{3}m$ structure of HS-PW does not fit with a sodium content of 1.54(5) per f.u. as confirmed by a meta-study of the PBA literature stating that there are no single phase materials existing when the sodium content is 1.5 [26]. Thus, a sodium content of 1.52(5) would rather result in a mixture of rhombohedral $R\bar{3}$ and cubic $Fm\bar{3}m$ phases detected

by XRD. Since all the Mössbauer spectra of the samples could be assigned to originate from iron-based PBAs, the true sodium content for the samples was determined (assuming no other charge compensation from different anions and cations present in the porous structure). This also implies that the amorphous impurity does not contain any iron. Therefore, for both FS-PW and HS-PW, there is an excess of sodium of ~ 0.5 per f.u. For DS-PW, there is an excess of ~ 0.2 indicating that the desodiation process using NO_2BF_3 may have removed some of the amorphous impurities. Electrochemical cycling of FS-PW (Figure S7) revealed an initial capacity from the first cycle of 155 mAh/g corresponding to 1.8 sodium-ions per f.u. which agrees well with the sodium content determined from Mössbauer spectroscopy. The excess sodium compound is most likely responsible for the surface deposits observed in the SEM images of FS-PW and HS-PW (Figure S4A-D). On the other hand, there are no surface deposits observed in the SEM image of DS-PW (Figure S4E-F), which also matches the lower excess of sodium relative to the two other samples. For PB-1, an excess of sodium of ~ 0.3 was found. The identity of the compound is not known. For all three PW samples, the combination of the characterization methods reveals $[Fe(CN)_6]^{n-}$ vacancy-free samples with well-quantified sodium and water content, while for the PB-1 sample 25% $[Fe(CN)_6]^{n-}$ vacancies was determined with no sodium present. Thus, the PALS results can reliably be related to the internal porosity of the samples.

From the PALS results, an increase in the average positron lifetime is observed when the sodium and water content decreases. The average lifetime increases further when $[Fe(CN)_6]^{n-}$ vacancies are present in the sample. Thus, the method can reliably correlate the average positron lifetime to the degree of filling of the crystal channels. However, the method does not provide evidence for which features/defect-complexes of the samples the detected positron lifetime components are related to; successive filling of the open channels by sodium atoms and water molecules going from DS-PW to FS-PW and/or the presence of $[Fe(CN)_6]^{n-}$ vacancies in varying concentrations (PB-1 vs. the PW samples). Two positron lifetimes were observed, where the 205 ps lifetime is stable for all four samples indicating that the positron experiences a cavity within the structure that is present in all four samples independent of the sodium, water, and/ or $[Fe(CN)_6]^{n-}$ vacancy content. A possible explanation

for the very stable 205 ps component could be the presence of water. For both FS-PW, HS-PW, and PB-1, the water content is high, which increases the possibility of having several water molecules close to each other within the structure. Since H_2O and Na^+ have the same electron density, they appear similar to the positron. Even a small amount of water present in the DS-PW sample would give rise to the 205 ps lifetime. In addition, the PB-1 and DS-PW sample are comparable when the 205 ps component is fixed giving rise to a third component with a very small intensity. On the other hand, the 405 ps lifetime changes with changing sodium, water, and/or $[Fe(CN)_6]^{n-}$ vacancy content. The second lifetime component seems to correlate with the degree of filling in the channels of the PW samples. When this component is set free, the lifetime value decreases from (458.4 ± 2.0) ps to (369.3 ± 1.3) ps with an increasing degree of filling in the channels. Fixing the component at 405 ps to compare the intensities shows that the intensity increases from FS-PW to DS-PW. This agrees well with emptying the open channels in the porous framework. For PB-1, a high intensity third component at ~ 514 ps was found. This could be due to the $[Fe(CN)_6]^{n-}$ vacancies (shown with curved dotted lines in Fig. 1) since the proportion of these vacancies in the sample is quite high. With a high defect density, most positrons should be unable to travel long diffusion paths due to trapping in the defects, so surface effects are unlikely despite the small particle size in PB-1.

Even though it is possible to observe quite large changes in the average positron lifetime between the four samples, it remains an open question if it is possible to decouple the effect of sodium, water, and/or $[Fe(CN)_6]^{n-}$ vacancies on the different positron lifetimes. Furthermore, the accuracy of the PALS method relative to other standard methods such as ICP and Mössbauer spectroscopy needs further investigation. The sensitivity of the PALS method for mono-vacancies in, i.e., metals is in the range of 1 ppm to 0.001%, thus, the sensitivity transfer to $[Fe(CN)_6]^{n-}$ vacancies in PBAs is not straight forward. This study also further strengthens the capability of Mössbauer spectroscopy to provide reliable and complementary information to other standard characterization methods. The combination of ICP, TGA, XRD, and Mössbauer spectroscopy is very powerful for determining the compositions and structures of PBAs, thus, they should be used when characterizing PBAs.

Conclusion

Since the performance of PBAs for various applications is linked to the internal porosity, the applicability of positron annihilation lifetime spectroscopy for determining the internal porosity of PBA cathode materials was investigated. Four samples, of which three had similar $[Fe(CN)_6]^{n-}$ vacancy content but changing sodium and water content, and one had 25% $[Fe(CN)_6]^{n-}$ vacancies but no sodium present, were examined. The filling of the open channel in the porous framework was found to influence the measured positron lifetime significantly. This could be correlated to the composition determined from ICP, TGA, and Mössbauer spectroscopy and the structure determined by XRD. The large gap between the average lifetimes of the individual samples provides a larger compositional space to examine in future studies. Thus, a good correlation between the cation, water, and/or $[M'(CN)_6]^{n-}$ vacancy in PBAs and the positron lifetime seems achievable. However, for future studies, it is also strongly suggested to update the PALS method to be performed under inert conditions. Furthermore, this work shows the importance of combining several characterization techniques to unravel the true composition of PBAs. Especially, Mössbauer spectroscopy provided a more accurate view of the composition of iron-based PBAs.

Acknowledgements

Author Contributions

IN contributed to conceptualization, data curation, formal analysis, investigation, project administration, visualization, writing—original draft, writing—review and editing. DB contributed to conceptualization, data curation, formal analysis, investigation, project administration, visualization, writing—original draft,

writing—review and editing. AB contributed to conceptualization, data curation, investigation, project administration, and visualization. TE contributed to formal analysis, investigation, and visualization. LH contributed to formal analysis, investigation, and visualization. WRB contributed to conceptualization, formal analysis, funding acquisition, supervision, writing—review and editing. TS contributed to supervision, formal analysis, writing—review and editing. RY contributed to funding acquisition, and supervision.

Funding

Data and code availability

The data can be accessed upon request.

Declarations

Conflict of interest   W.R.B and R.Y. are co-founders of the company ALTRIS AB, which produces Prussian white powder for sodium-ion battery applications.

Ethical approval   No ethical approval was needed for this study.

Supplementary Information   The online version contains supplementary material available at https://doi.org/10.1007/s10853-023-09025-x.

References

[1] Wang L et al (2015) Rhombohedral Prussian white as cathode for rechargeable sodium-ion batteries. J Am Chem Soc 137:2548–2554

[2] Bauer A et al (2018) The scale-up and commercialization of nonaqueous Na-ion battery technologies. Adv Energy Mater 8:1–13

[3] Asakura D et al (2012) Fabrication of a cyanide-bridged coordination polymer electrode for enhanced electrochemical ion storage ability. J Phys Chem C 116:8364–8369

[4] Wu X et al (2013) Single-crystal $FeFe(CN)_6$ nanoparticles: a high capacity and high rate cathode for Na-ion batteries. J Mater Chem A 1:10130–10134

[5] Rudola A, Du K, Balaya P (2017) Monoclinic sodium iron hexacyanoferrate cathode and non-flammable glyme-based electrolyte for inexpensive sodium-ion batteries. J Electrochem Soc 164:A1098–A1109

[6] Ganguli S, Bhattacharya M (1983) Studies of different hydrated forms of Prussian Blue. J Chem Soc Faraday Trans 1 Phys Chem Condens Phases 79:1513–1522

[7] Brant WR et al (2019) Selective control of composition in Prussian white for enhanced material properties. Chem Mater 31:7203–7211

[8] Dlubek G, Lademann P, Krause H, Krause S, Unger R (1998) Positron lifetime studies of decomposition in 2024 (Al-Cu-Mg) and 7010 (Al-Zn-Cu-Mg) alloys. Scr Mater 39:893–899

[9] Staab TEM, Krause-Rehberg R, Kieback B (1999) Positron annihilation in fine-grained materials and fine powders: an application to sintering of technically used metal powders. J Mater Sci 34:3833–3851. https://doi.org/10.1023/A:1004666003732

[10] Liu D et al (2022) Microstructure modulation of Zn doped $VO_2(b)$ nanorods with improved electrochemical properties towards high performance aqueous batteries. Batteries 8:172, 1–11

[11] Zhu K et al (2021) Defect engineering on V_2O_3 cathode for long-cycling aqueous zinc metal batteries. Nat Commun 12:6878, 1–9. https://doi.org/10.1038/s41467-021-27203-w

[12] Brunner P, Steyskal E-M, Topolovec S, Würschum R (2022) Positronium chemistry of a $Fe^{2+/3+}$ solution under electrochemical control. J Chem Phys 157:234202, 1–11

[13] Coelho AA (2018) TOPAS and TOPAS-academic: an optimization program integrating computer algebra and crystallographic objects written in C^{++}. J Appl Crystallogr 51:210–218

[14] Haaks M (2003) Positronenspektroskopie an Ermüdungsrissen und Spanwurzeln. Ph.D. thesis, HISKP, Universität Bonn, Nußallee 14–16, D-53115 Bonn, Germany

[15] Petschke D, Staab TE (2019) DDRS4PALS: a software for the acquisition and simulation of lifetime spectra using the DRS4 evaluation board. SoftwareX 10:100261, 1–10

[16] Ritt S (2008) Design and performance of the 6 GHz waveform digitizing chip DRS4, pp 1512–1515 (19.10.2008–25.10.2008)

[17] Software download for the DRS4 evaluation board (2018). https://www.psi.ch/drs/software-download

[18] Petschke D (2021) dpscience/dquickltfit: Dquickltfit v4.2 (version 4.2). https://doi.org/10.5281/zenodo.4461707

[19] Kirkegaard P, Eldrup M (1972) Positronfit: a versatile program for analyzing positron lifetime spectra. Comput Phys Commun 3:240–255

[20] Markwardt CB (2009) Non-linear least squares fitting in IDL with MPFIT. In: Proceedings ADASS XVIII. arXiv: 0902.2850v1

[21] Levenberg K (1944) A method for the solution of certain non-linear problems in least squares. Q Appl Math 2:164–168

[22] Marquardt DW (1963) An algorithm for least-squares estimation of nonlinear parameters. J Soc Ind Appl Math 11:431–441

[23] Aparicio C, Machala L, Marusak Z (2012) Thermal decomposition of Prussian blue under inert atmosphere. J Therm Anal Calorim 110:661–669

[24] Nielsen I et al (2022) Water driven phase transitions in Prussian white cathode materials. J Phys Energy 4:044012, 1–10

[25] Ojwang DO, Häggström L, Ericsson T, Angström J, Brant WR (2020) Influence of sodium content on the thermal behavior of low vacancy Prussian white cathode material. Dalton Trans 49:3570–3579

[26] Boström HLB, Brant WR (2022) Octahedral tilting in Prussian blue analogues. J Mater Chem C 10:13690–13699

[27] Chen J et al (2020) Prussian blue, its analogues and their derived materials for electrochemical energy storage and conversion. Energy Storage Mater 25:585–612

[28] Ojwang DO et al (2021) Moisture-driven degradation pathways in Prussian white cathode material for sodium-ion batteries. ACS Appl Mater Interfaces 13:10054–10063

[29] Ericsson T, Häggström L, Ojwang DO, Brant WR (2022) Investigation of valence mixing in sodium-ion battery cathode material Prussian white by Mössbauer spectroscopy. Front Energy Res 10:909549, 1–6

[30] Reguera E, Fernández-Bertrán J, Dago A, Díaz C (1992) Mössbauer spectroscopy study of Prussian blue from different provenances. Hyperfine Interact 73:295–308